All-photonic synapse based on iron-doped lithium niobate double metal-cladding waveguides

Qiheng Wei,[1,*] Hailang Dai,[1,*,†] Hongrui Shan,[1] Honggen Li,[1] Zhuangqi Cao,[1] and Xianfeng Chen[1,2,‡]

[1]*State Key Laboratory of Advanced Optical Communication Systems and Networks, School of Physics and Astronomy, Shanghai Jiao Tong University, Shanghai 200240, China*

[2]*Collaborative Innovation Center of Light Manipulations and Applications, Shandong Normal University, Jinan 250358, China*

(Received 21 June 2021; revised 28 October 2021; accepted 10 December 2021; published 27 December 2021)

In an artificial neural network composed of neuromorphic computing units, the resistance of the memristor can be modulated dynamically and repeatedly under external stimuli, such as electric fields, magnetic fields, and light illumination, leading to variations in local conductivity and memory effects. Here we show, using an all-photonic memristor, that the memristance arises naturally in an optical system in which solid-state ionic transport is realized under low-power external incident light. These results show an extremely stable multilevel storage weight and a high signal-to-noise ratio. In all-photonic memristors, the light signal is employed as the extra stimuli of the memristor devices to ensure a large memory window and a variation margin of multiple storage levels.

DOI: 10.1103/PhysRevB.104.235308

I. INTRODUCTION

Nowadays, with the rapid development of "big data" technology [1], the gradual failing of Moore's law and the constraint of the Von Neumann bottleneck hinder the computing ability of "big data" applications with random-access memory and photolithography. As a result, it is highly desirable to seek ways to increase computing power, which presents a great challenge to the traditional von Neumann architecture. Compared with electronic computing systems, the human brain excels at learning, recognizing, and classifying, due to its unified memory and processing unit [2,3]. Inspired by human brain processing, neuromorphic computing is considered to be an efficient and powerful approach to filling the subsequent power vacuum in the post-Moore era. In an artificial neural network composed of neuromorphic computing units, the memristor, of which the resistance can be modulated dynamically and repeatedly under external stimuli (such as electric fields [4], magnetic fields [5], and light illumination [4]), plays as important a role as neurons do in the human brain. Therefore, plenty of work has been performed to exploit excellent memristors, including electronic memristors due to electrically induced resistive changes [6–11], and photonic memristors of which the storage layer depends on the external photonic signal [12–15]. Therein, photonic memristors are characterized by an unprecedented bandwidth and high speed in storing and processing data via optical means [16–21]. However, the physical mechanism of existing photonic memristors relies on resistive switching devices [22–24], in which different intensities of optical signals are transformed to the resistance transitions between high and low resistance states, causing difficulty in integration due to the photoelectric conversion and opaque electrode. Moreover, on-chip photonic synapses are demonstrated based on phase-change materials and tapered waveguide [25,26], utilizing a high-intensity pulsed laser to heat the phase-change materials (PCMs) to the temperature over the melting point or between the crystal point and the melting point, which results in the probe light transmission change of the waveguide [27]. Nevertheless, the optical control of PCMs requires typically complex configurations based on pulsed, high-intensity laser systems, and the quantity of heat during the crystallization and amorphous process may accumulate gradually, leading to instability and an absence of recoverability. In addition, the transmission does not change a lot with different crystallinity, implying a low signal-to-noise ratio.

Here, we demonstrate an all-photonic memristor based on a double metal-cladding waveguide (DMCW) composed by a middle iron-doped lithium niobate (IDLN) guided layer and two terminal cladded silver film layers. In this method, two CW laser beams with different incident angle are applied to induce a different distribution of light field in the IDLN guided wave layer, causing a different refractive index change on account of the photorefractive effect [28], respectively. Meanwhile, the reflectivity of the DMCW is extremely sensitive to the refractive index change and can be steadily reconfigured by an incident beam with an absence of heat, achieving an extremely stable multilevel storage weight and a high signal-to noise ratio. All-photonic memristors utilize an optical signal as the neurotransmitter, and the information is stored and processed with the reflectivity of the device. Therefore, our all-photonic synapse can perform the same function as a natural synapse, and it has considerable potential to form an integrated and highly efficient neuromorphic computing system.

II. METHOD

A. Theory of the DMCW

The double metal-cladding waveguide (DMCW) is a three-layer structure, as shown in Fig. 1(a). From top to bottom,

*These authors contributed equally to this work.
†hailangdai@sjtu.edu.cn
‡xfchen@sjtu.edu.cn

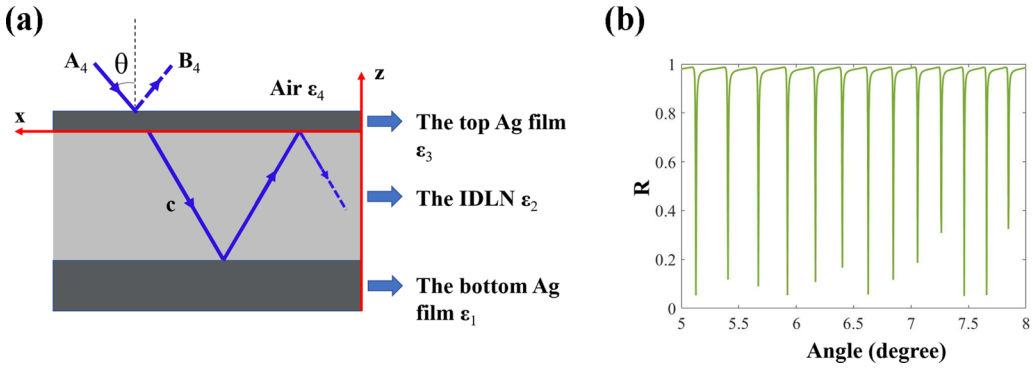

FIG. 1. (a) The three-layer structure of the DMCW. (b) The attenuated total reflection with a different incident angle. When the incident light satisfies the resonance condition, it will be coupled into the waveguide, resulting in resonance coupling peaks.

the layers are air, thin Ag film, iron-doped lithium niobate (IDLN), and thick Ag film. The thicknesses of the thin Ag film and IDLN are s and d, respectively, and the relative dielectric constants from the bottom Ag film to air are set as ε_1, ε_2, ε_3, and ε_4, respectively. Assuming the air layer and the thick Ag film layer extend at infinity, and the width of the guiding layer is much greater than its thickness, we can consider that the electric field in the waveguide is confined in only one direction, and we take it as the x direction. We also assume that the geometric structure and the refraction index distribution of the waveguide are constant in the y direction. For guided modes, the electric fields in the substrate and coating layers attenuate exponentially, and the electric field in the guided layer and air is an oscillating field consisting of two waves propagating in opposite directions. Consequently, for TE polarization, the electric field in the waveguide can be expressed as

$$E_y(z) = \begin{cases} A_4 \exp\left(-i\kappa_4(z-s)\right) + B_4 \exp\left(i\kappa_4(z-s)\right), & s < z < +\infty, \\ A_3 \exp\left(-p_3 z\right) + B_3 \exp\left(p_3 z\right), & 0 < z < s, \\ A_2 \exp\left(-i\kappa_2 z\right) + B_2 \exp\left(i\kappa_2 z\right), & -d < z < 0, \\ A_1 \exp\left(p_1(z+d)\right), & -\infty < z < -d, \end{cases} \tag{1}$$

where

$$\begin{aligned} p_1 &= \left(\beta^2 - {k_0}^2\varepsilon_1\right)^{1/2}, \\ \kappa_2 &= \left({k_0}^2\varepsilon_2 - \beta^2\right)^{1/2}, \\ p_3 &= \left(\beta^2 - {k_0}^2\varepsilon_3\right)^{1/2}, \\ \kappa_4 &= \left({k_0}^2\varepsilon_4 - \beta^2\right)^{1/2}. \end{aligned} \tag{2}$$

$k_0 = 2\pi/\lambda$ is the propagation constant in vacuum, and $\beta = k_0 n_0 \sin\theta$ is the x component of the wave vector k. Using the continuity condition of E_y and $\partial E_y/\partial z$ at boundaries $z = 0$, $z = s$, and $z = -d$, the reflection coefficient r can be expressed as

$$r = \frac{B_4}{A_4} = \frac{r_{43} + r_{321}\exp(-2p_3 s)}{1 + r_{43} r_{321}\exp(-2p_3 s)}, \tag{3}$$

where

$$\begin{aligned} r_{43} &= \exp(-2i\phi_{43}), \\ r_{321} &= \frac{\exp(-2i\phi_{23}) - \exp\left[2i(\kappa_2 d - \phi_{21})\right]}{\exp\left[2i(\kappa_2 d - \phi_{21} - \phi_{23})\right] - 1}, \\ \phi_{21} &= \tan^{-1}\left(\frac{p_1}{\kappa_2}\right), \\ \phi_{23} &= \tan^{-1}\left(\frac{p_3}{\kappa_2}\right), \\ \phi_{43} &= \tan^{-1}\left(\frac{p_3}{\kappa_4}\right). \end{aligned} \tag{4}$$

The reflectivity R is equal to $rr* = |r|^2$. For the DMCW, the reduced dispersion equation for the m-order eigenmode can be written as

$$k_0 d\sqrt{n^2 - N_{\text{eff}}^2} = m\pi, \tag{5}$$

where $N_{\text{eff}} = \beta/k_0$ is the effective refractive index. When the component along the propagation direction of the wave vector resonates with the propagation constant of the eigenmodes, the energy of the incident beam will be coupled into the waveguide, resulting in coupling peaks, as shown in Fig. 1(b). In this situation, incident beams will excite different eigenmodes in the guided layer and form a different field distribution, depending on its incident angle and wavelength. In addition, the refractive index of the guided layer will be changed by the field distribution, according to the photorefractive effect of the IDLN. When the refractive index of the guided layer is switched, the eigenmodes will also be switched, resulting in a changing resonance coupling efficiency of the probe beam. Therefore, the change of the refractive index around the incident point of the probe beam

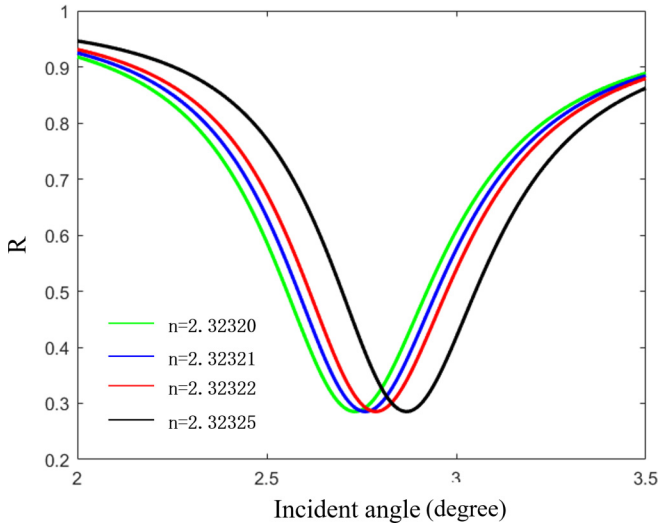

FIG. 2. Simulations with a different refractive index. When the refractive index of the guided layer increases 10^{-5}, the coupling peak will go through a detectable translation. We can read the refractive index as changing reflective intensity of the probe beam with a fixed incident angle.

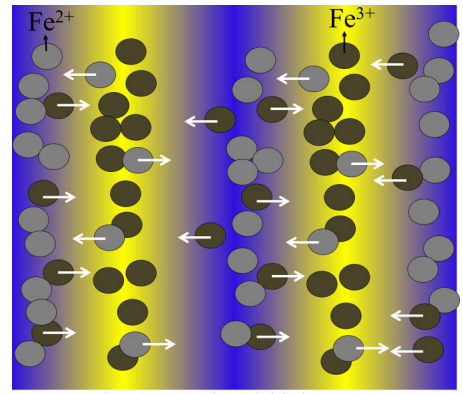

FIG. 3. The schematic of charge carrier drift. In IDLN, the dropped ferrous ions in the bright region will be excited to ferric ions with incident light, generating conduction-band electrons. Then the conduction-band electrons will drift to the dark region, and the ferric ions in the dark region will capture the electrons to become ferrous ions. Finally, the distribution of ferrous ions and ferric ions changed, forming inside electric field. The inside electric field will switch the refractive index of the IDLN by nonlinear effect.

can be read out as a change of the reflectivity of the probe beam.

Furthermore, compared with the conventional all-dielectric optical waveguides, the DMCW possesses a variety of fascinating optical properties [29–32]. The effective refractive index, N_{eff}, is particularly sensitive to the refractive index that the sensitivity s is defined as,

$$s = dN_{\text{eff}}/dn = n/N_{\text{eff}}, \tag{6}$$

where the sensitivity approaches infinity with N_{eff} approaching zero in UOMs [31].

Figure 2 presents the change of reflectivity with a different refractive index guided layer in which the resonance coupling peak will translate with increasing refractive index, and it is shown that a 10^{-5} refractive index change is detectable [33,34], indicating a high signal-to-noise ratio [25].

B. Refractive index switched by incident light

If the light illuminates the upper silver film under the coupling condition, the energy of the incident light will be coupled into eigenmodes of the DMCW, and it will then form a modulated field distribution. The modulated distribution of the field will drive the photorefractive effect, and the ferrous ions in the bright region will drift to the dark region while the density of ferric ions in the dark region will drift to the bright region (actually, the ion drift is realized by the transmission of the conduction-band electrons), as shown in Fig. 3. During the redistribution process, the inside electric field will increase, causing a gradually increased current that is contrary to the light-induced ion drift. When the influence of the erasing light field and the inside electric field is canceled out, the device will reach a stable state, called a baseline state.

In this work, two 532 nm laser beams with incident angles θ_1 and θ_2 are, respectively, applied to form two different standing-wave field distribution, as shown in Fig. 4(a). The incident points of the two beams are close but not coincident. In the two baseline states induced by the two incident beams (labeled $L1$ and $L2$), the refractive index of the guided layer around the incident point of the probe beam is different. Therefore, with an incident beam of angle θ_2, the refractive index of the guided layer will gradually change to the refractive index of state $L2$, and with an incident beam of angle θ_1, the refractive index of the guided layer will also change to the refractive index of state $L1$. As a result, information can be recorded into the device by switching the refractive index with two incident beams. In addition, with the sensitivity of the DMCW to the refractive index change, the information can be read out as different reflective intensity varying between the high and low reflectivity states, as shown in Fig. 4(b).

As shown in Fig. 4(b), with an incident beam of angle θ_1, the sample will go through a conversion from $L2$ to $L1$, and vice versa. The variation range of the probe beam reflectivity is larger than 25%, which is influenced by the coupling efficiency of the DMCW (the readout of a 100% coupling efficiency DMCW will vary from 1 to 0 with the change of the refractive index). This physical mechanism allows the device to realize the same function as the traditional memristors, namely that the reflectivity characterizes the incident optical signal.

III. EXPERIMENTAL SETUP

The experiment setup is shown in Fig. 5. A 532 nm CW laser beam is split into three parts, a part of the beam as a calibration beam used to monitor the source power, and the other part labeled probe beam used to probe the reflectivity and erase the sample to the initial $L1$ state, and the third beam called recording beam used to record data into the device. Two light shutters (SH05/M) are applied to accurately control the illumination time, as presented in Fig. 5(a). And the intensity of reflected light is collected and measured by a photoelectric detector. Figure 5(b) shows the attenuated total reflection

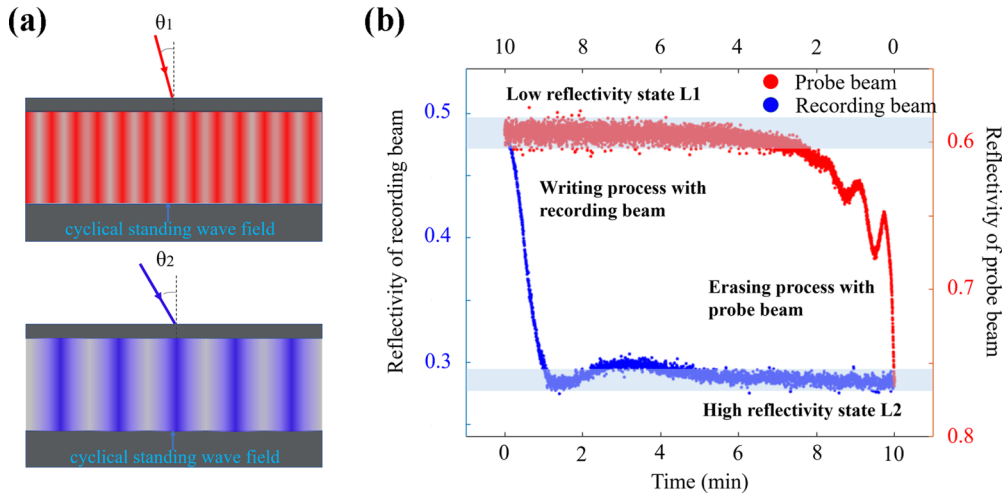

FIG. 4. Schematic of the different standing-wave modes in the guided layer and the changing reflectivity of the photorefractive process in the recording and erasing process. (a) Different incident light beams with angles θ_1 and θ_2 will excite different standing-wave modes. (b) The probe light with incident angle θ_1 will urge the device to reach a stable state $L1$ due to the photorefractive effect. Under the illumination of recording light with incident angle θ_2, the device will go through a conversion from state $L1$ to $L2$. Therefore, the property of the all-photonic synapses can be switched between states $L1$ and $L2$ with probe and recording light, indicating a similar physical mechanism to the electronic memristors.

(ATR) of the device and the schematic of the reflect light is presented in Fig. 5(c). The memristor consists of two terminal cladded silver film layers (30 nm for the former, 300 nm for the later), and a 0.5-mm-thick IDLN (0.3%) guided layer, as presented in Figs. 5(d) and 5(e). The IDLN crystal is Z-cut, in which the z-axis direction is along the vertical direction, and the x and y axes lie along the 9 mm and the 10 mm direction, respectively. The electric field distribution in the guided layer is shown in Fig. 5(f) that the incident light excites cyclical standing wave in the DMCW. Before recording data, the de-

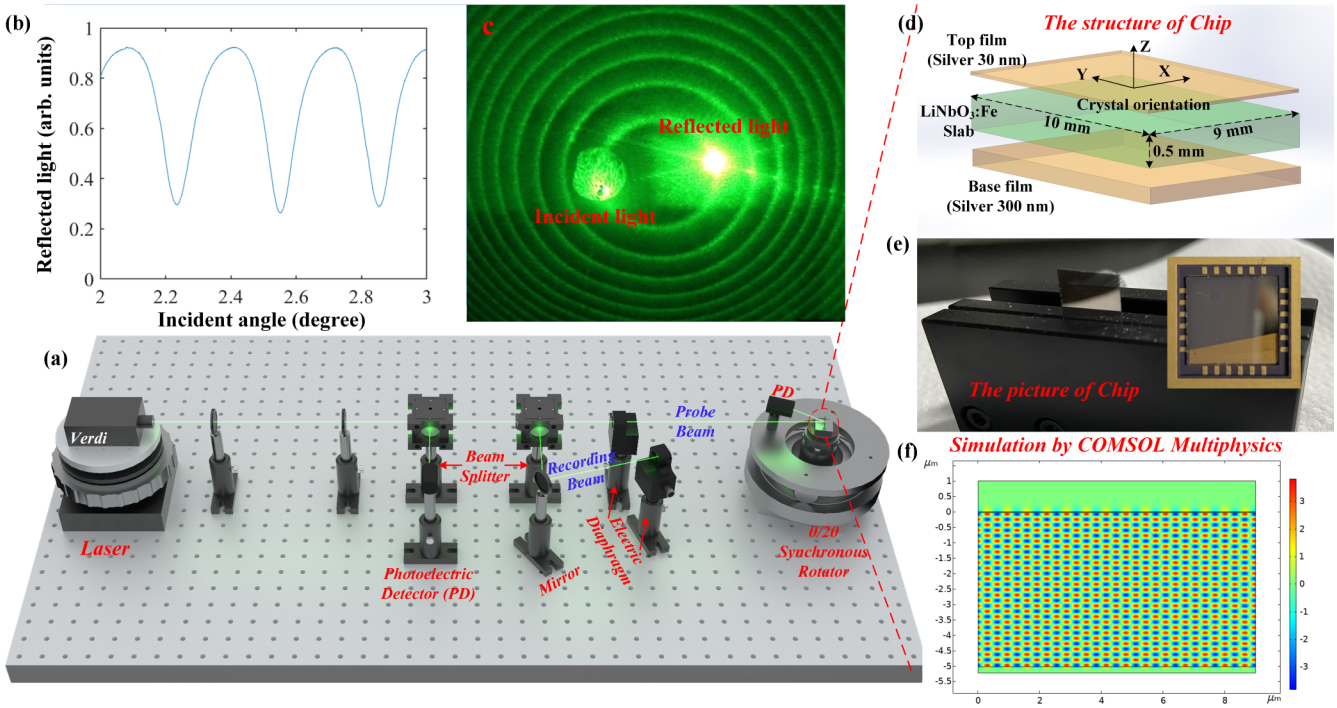

FIG. 5. The experimental setup. (a) A 100 mW 532 nm laser beam is divided into three parts: the calibration beam (27.8 mW), the probe beam (28.1 mW), and the recording beam (16.2 mW). The illumination time is controlled by two light shutters (Thorlab SH05/M), and a turntable with a photoelectric detector is used to rotate the synapse and measure the reflected light. (b) The attenuated total reflection (ATR) of the device. (c) The schematic of the reflected light. (d) The synapse consists of three layers: a 0.5-mm-thick IDLN (0.3%) layer is used as guided layer, a 30-nm-thick silver film is used to couple the incident light, and another 300-nm-thick silver film serves as the substrate layer. (e) An image of the device. (f) The schematic of the electric field distribution in the guided layer, simulated by COMSOL MULTIPHYSICS.

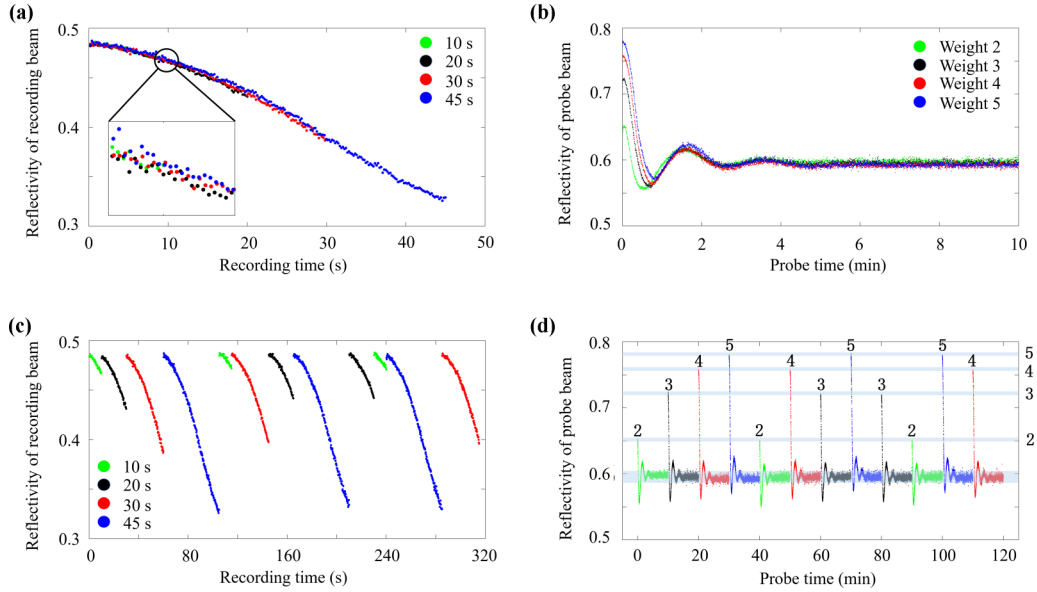

FIG. 6. The results of the 0.5 mm device under a 100 mW 532 nm laser source. (a) The reflectivity change of the recording light in the recording process from the state $L1$ with 10, 20, 30, and 45 s illumination of the recording light. The corresponding weights are labeled as 2, 3, 4, and 5. (b) The readout of the reflectivity changing for weight 2, 3, 4, and 5. (c) The reflectivity change of the recording light in a series of weight 2-3-4-5-2-4-3-5-3-2-5-4. (d) The corresponding readout of the probe light reflectivity in the series of weight switch 2-3-4-5-2-4-3-5-3-2-5-4.

vice is set to the $L1$ state with 10 min illumination of the probe light. The reflectivity of the probe light in the saturated $L1$ state is defined as the baseline state to a weight "1." From the baseline state, the reflectivity of the probe beam can change to weight "2," "3," "4," and "5" with 10, 20, 30, and 45 s illumination of the recording light, respectively. To decrease the weight, the device is completely erased to the baseline state $L1$ with 10 min probe beam illumination, making it a piece of white paper which can be rewritten again for many times. Meanwhile, the storage weight can be more subdivided by reduced illumination time interval, due to the high signal-to-noise ratio in the memristor. As a result, the multilevel storage weight of the device can be stably and repeatedly switched due to the excellent sensitivity to the refractive index change and can be steadily reconfigured by incident beam with absence of heat. In the following part, the fascinating performances of the memristor have been presented.

IV. RESULTS AND DISCUSSION

A. Results of the recording and erasing process

Figure 6(a) presents the recording process in which the device is recorded to weight 2 (green), 3 (black), 4 (red), and 5 (blue) from the baseline state with 10, 20, 30, and 45 s illumination of the recording light. The readout and erasing process is shown in Fig. 6(b), which indicates that the reflectivity of the probe beam changes to four clearly distinguishable states with different input recording beam illuminations. Therefore, with the erasing and recording beam, the device can be switched between five clearly distinguishable states. To demonstrate that the reflectivity change is stable, repeatable, and entirely unrelated to the previous weight of the device, we extended our experiment in which a series of weight changes 2-3-4-5-2-4-3-5-3-2-5-4 is performed, where the device is erased by a 10 min probe illumination after each recording process, as shown in Figs. 6(c) and 6(d). It is shown that the readout with the same input signal will change to a stable and clearly distinguished level from the baseline state regardless of the device's previous state. The timescale of the erasing process is larger than the recording process to reach a stable baseline state. In addition, in order to test the stability of the baseline state, we extend the irradiation time of the probe beam resulting in the reflectivity change process given in minutes. Consequently, our all-photonic memristor is demonstrated with stable and repeatable multilevel storage weights.

B. Recording accuracy

To investigate the accuracy of the recording time, research with different time intervals is also carried out, as shown in Fig. 7. Figures 7(a) and 7(b) show the recording process with an incident signal of 5, 10, 15, and 20 s, and its corresponding readout with 10 min probe light illumination. It is a distinctly different readout with a time interval of 5 s. In Figs. 7(c) and 7(d), the device is recorded with a signal of 2, 4, 6, and 8 s, and erased with 10 min probe light illumination, where the readout is barely distinguishable. Hence, the time accuracy is about 2 s, indicating that the recording process can be cut into more stable and distinguishable fragmentary states.

C. Discussion of the response time

In particular, the photorefractive effect of the IDLN is based on the drifting of the charge carrier. In the guided layer of DMCW, the charge carriers are driven by the intensity gradient field of the standing wave. To uncover the influence of the guided layer thickness and the intensity of incident light, experiments on a thinner guided layer and lower light source power are implemented. As shown in Figs. 8(a) and

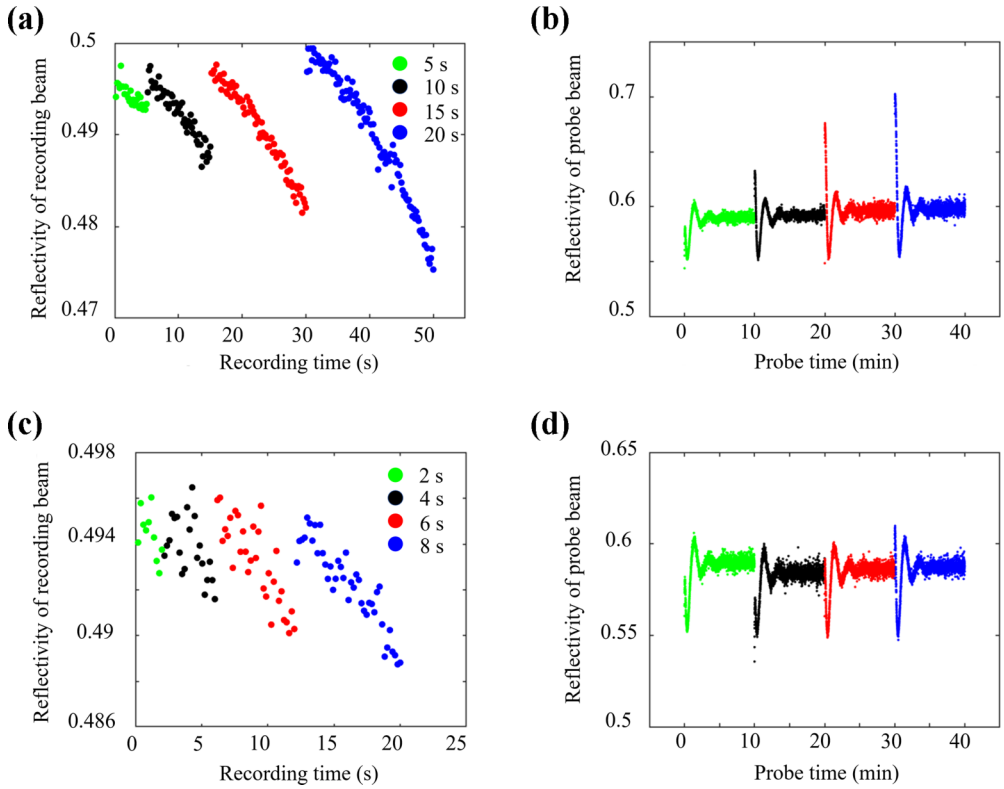

FIG. 7. (a), (b) The reflectivity change of the recording light from the baseline state with 5, 10, 15, and 20 s illumination of the recording light and its corresponding readout. (c), (d) The reflectivity change of the recording light from the baseline state with 2, 4, 6, and 8 s illumination of the recording light and its corresponding readouts.

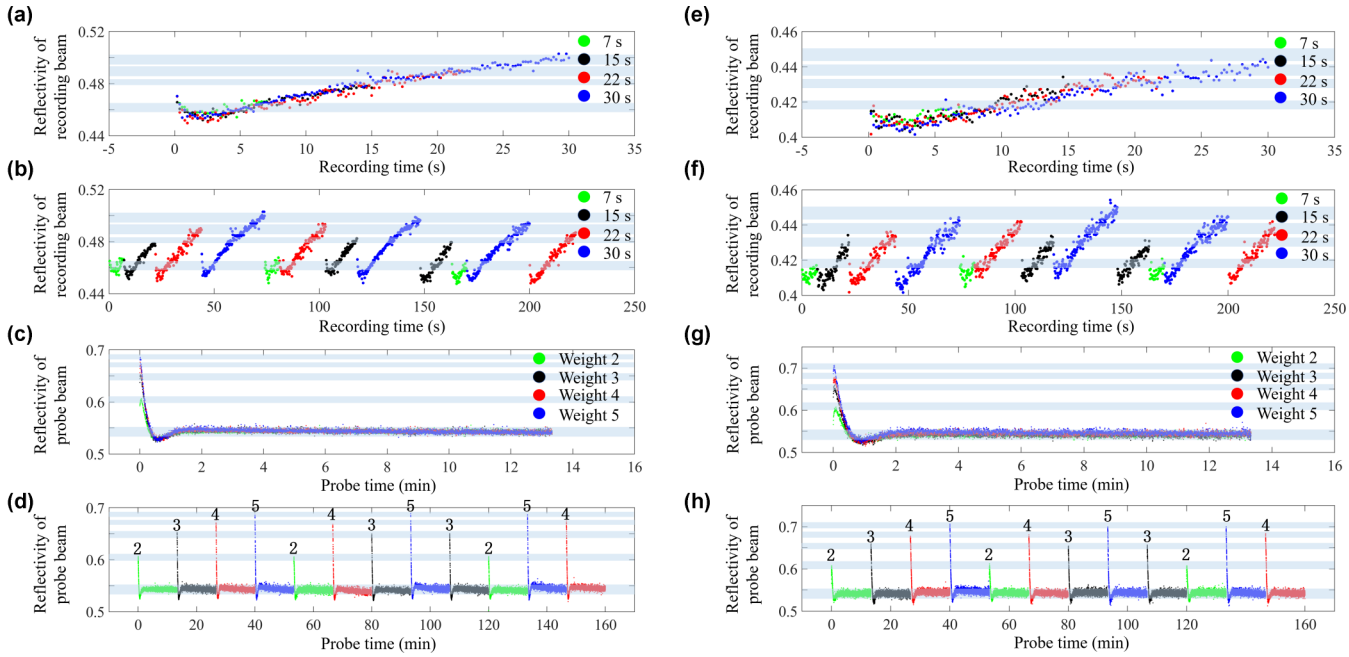

FIG. 8. (a)–(d) Results with a 100 mW light source and a 0.3-mm-thick device. (a) The reflectivity change of the recording light in the recording process from the state $L1$ with 7, 15, 22, and 30 s illumination of the recording light. The corresponding weights are labeled 2, 3, 4, and 5. (b) The reflectivity change of the recording light in a cycle of weight 2-3-4-5-2-4-3-5-3-2-5-4. (c) The readout of the reflectivity change in weight 2, 3, 4, and 5. (d) The corresponding readout of the probe light reflectivity in the series of weight switch 2-3-4-5-2-4-3-5-3-2-5-4. (e)–(h) Results with a 70 mW light source and a 0.3-mm-thick device. (e) The reflectivity change of the recording light in the recording process from the state $L1$ with 7, 15, 22, and 30 s illumination of the recording light. The corresponding weights are labeled 2, 3, 4, and 5. (f) The reflectivity change of the recording light in a cycle of weight 2-3-4-5-2-4-3-5-3-2-5-4. (g) The readout of the reflectivity change in weight 2, 3, 4, and 5. (h) The corresponding readout of the probe light reflectivity in the series of weight switch 2-3-4-5-2-4-3-5-3-2-5-4.

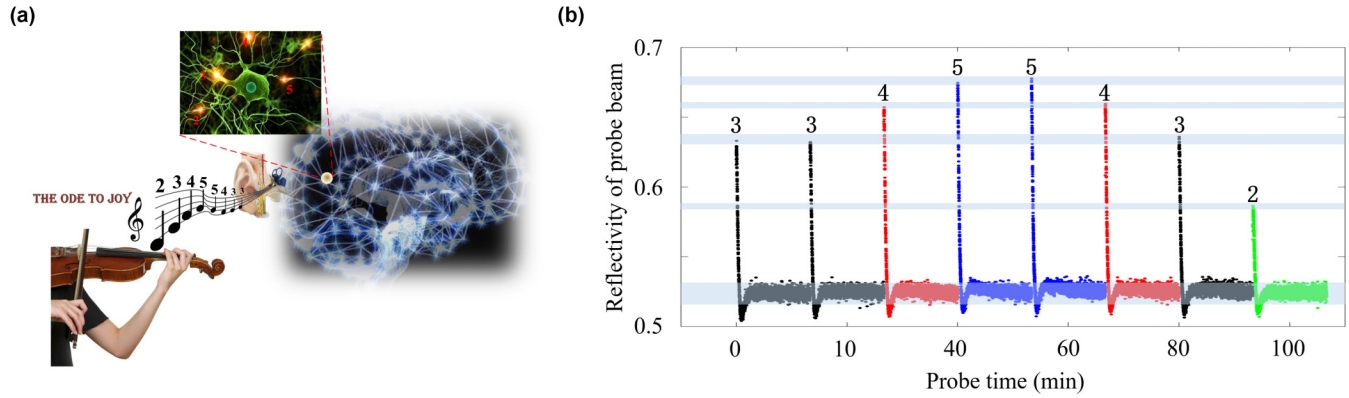

FIG. 9. (a) Schematic of the recording process of Beethoven's Ode to Joy. (b) Its corresponding readout.

8(b), and Figs. 8(e) and 8(f), the device can also achieve stable and repeatable multilevel storage weights. Figures 8(d) and 8(h) show that all preset storage weights can be reached repeatedly. In the experimental results, the device with a 0.3-mm-thick guided layer under a 100 mW laser source will achieve the $L1$ state faster with 1.8 min probe illumination shown in Fig. 8(c), in contrast with 4.8 min for the 0.5-mm-thick guided layer device shown in Fig. 8(g). The reduction of the light source power will decrease the intensity contrast ratio in the IDLN, causing an extension of the erasing time (about 2.5 min for a 0.3 mm guided layer device under a 70 mW laser source). Therefore, a thin film device is expected to achieve a rapid switching process and stable multilevel storage weight. According to the experimental results, the DMCW memristor provides a way to realize the same functional capability as the synapses in the human brain, which are characterized by memory and processing properties with strongly plasticity. To demonstrate the memory property, the first part of Beethoven's Ode to Joy is recorded into the device step-by-step, and quickly read out by probe light, as shown in Fig. 9(a). This implies that our all-photonic memristor is capable of performing the same function as the synapses in the human brain; the results are shown in Fig. 9(b).

D. Comparison of the realized device with similar solutions

A comparison of the realized device with similar solutions is shown in Table I. Our device is an all-photonic device in which the storing, processing, and conversion of the data are all done in a photonic way, extricating it from the restriction of the opaque electrode. Compared with other all-photonic devices, the physical mechanism is the photorefractive effect, and the DMCW is switched by a CW laser, indicating a switching process without pulse laser-induced damage and heating. In addition, the variety range of the weight in DMCW is larger due to the sensitivity to the refractive index change.

V. CONCLUSIONS

In this work, we proposed a DMCW based on IDLN which is demonstrated with repeatable stable multilevel storage weights. Compared with other photonic memristors, the storing, processing, and conversion of the data in our device are fully photonic with the absence of heat and photoelectric conversion, extricating it from restriction of the thermal disturbance and the opaque electrode. We use the 532 nm CW laser for the recording and reading process, aiming to show the writing and erasing properties of the device. In future work, the probe beam can be replaced by a long-wavelength laser where IDLN is no longer photosensitive so that the information can be read out steadily without erasing effect. Moreover, the variation range of the probe reflectivity is larger than 25%, which can be further improved with high coupling efficiency DMCW. We also investigated the accuracy of the recording time, and the physical mechanism of the response time is discussed, indicating that a thin film device is expected to achieve a rapid switching response. As a result, our all-photonic synapse is characterized by extremely excellent properties, presenting a considerable potential to form an integrated and efficient neuromorphic computing system.

ACKNOWLEDGMENTS

Funding for this work was from the National Key R&D Program of China (Grants No. 2017YFA0303701 and No.

TABLE I. Comparison of the realized device with similar solutions.

Structure	Stimuli	Memory mechanism	Physical mechanism	R_{on}/T_{on}	R_{off}/T_{off}
DMCM	CW laser	Reflectivity switch	Photorefractive effect	T_{on}: 0.48	T_{off}: 0.28
Tapered waveguide [25]	Pulsed laser	Transmissivity switch	Phase change material	T_{on}:1.07T_0	T_{off}: T_0
Waveguide GST element [35]	Pulsed laser	Transmissivity switch	Phase change material	T_{on}:1.2T_0	T_{off}: T_0
ITO/CeO_{2-X}/AlO_y/Al [16]	Pulsed laser	Resistance switch	Photoconductivity effect	R_{on}/R_{off} ratio ~14	
MoS_2 RRAM [36]	uv light/Voltage	Resistance switch	Photoconductivity effect	R_{on}/R_{off} ratio ~12	
Pt/TiO_2/Pt [6]	Voltage	Resistance switch	Charged dopants drift	R_{on}/R_{off} ratio ~380	

2018YFA0306301); the National Natural Science Foundation of China (NSFC) (Grants No. 11734011, No. 11764020, and No. 11974245); the Foundation for the fellowship of China Postdoctoral Science Foundation (Grants No. 2020M681275 and No. 2021T140452); and the Shanghai Municipal Science and Technology Major Project (Grant No. 2019SHZDZX01).

[1] M. I. Jordan and T. M. Mitchell, Science **349**, 255 (2015).
[2] E. R. Kandel, J. H. Schwartz, T. M. Jessell, S. A. Siegelbaum, and A. J. Hudspeth, *Principles of Neural Science* (McGraw-Hill, New York, 2013).
[3] G. Indiveri and S. C. Liu, Proc. IEEE **103**, 1379 (2015).
[4] Y. C. Yang and R. Huang, Nat. Electron. **1**, 274 (2018).
[5] D. P. Sahu and S. N. Jammalamadaka Remote, Sci. Rep. **7**, 17224 (2017).
[6] D. B. Strukov, G. S. Snider, D. R. Stewart, and R. S. Williams, Nature (London) **453**, 80 (2008).
[7] C. D. Wright, Y. W. Liu, K. I. Kohary, M. M. Aziz, and R. J. Hicken, Adv. Mater. **23**, 3408 (2011).
[8] D. Kuzum, R. G. D. Jeyasingh, B. Lee, and H. S. P. Wong, Nano Lett. **12**, 2179 (2012).
[9] T. Tuma, A. Pantazi, M. Le Gallo, A. Sebastian, and E. Eleftheriou, Nat. Nanotechnol. **11**, 693 (2016).
[10] B. Gao, Y. Bi, H. Y. Chen, R. Liu, P. Huang, B. Chen, L. Liu, X. Liu, S. Yu, H. S. P. Wong, and J. Kang, ACS Nano **8**, 6998 (2014).
[11] C. Wu, T. W. Kim, H. Y. Choi, D. B. Strukov, and J. J. Yang, Nat. Commun. **8**, 752 (2017).
[12] W. Xu, H. Cho, Y. H. Kim, Y. T. Kim, C. Wolf, C. G. Park, and T. W. Lee, Adv. Mater. **28**, 5916 (2016).
[13] B. Gholipour, P. Bastock, C. Craig, K. Khan, D. Hewak, and C. Soci, Adv. Opt. Mater. **3**, 635 (2015).
[14] H. Tan, G. Liu, X. Zhu, H. Yang, B. Chen, X. Chen, J. Shang, W. D. Lu, Y. Wu, and R. W. Li, Adv. Mater. **27**, 2797 (2015).
[15] G. Agnus, W. Zhao, V. Derycke, A. Filoramo, Y. Lhuillier, S. Lenfant, D. Vuillaume, C. Gamrat, and J. P. Bourgoin, Adv. Mater. **22**, 702 (2010).
[16] H. Tan, G. Liu, H. Yang, X. Yi, L. Pan, J. Shang, S. Long, M. Liu, Y. Wu, and R. W. Li, ACS Nano **11**, 11298 (2017).
[17] K. Pei, X. Ren, Z. Zhou, Z. Zhang, X. Ji, and P. K. L. Chan, Adv. Mater. **30**, 1706647 (2018).
[18] J. Gorecki, V. Apostolopoulos, J. Y. Ou, S. Mailis, and N. Papasimakis, ACS Nano **12**, 5940 (2018).
[19] Y. Shen, N. C. Harris, S. Skirlo, M. Prabhu, T. Baehr-Jones, M. Hochberg, X. Sun, S. Zhao, H. Larochelle, D. Englund, and M. Soljačić, Nat. Photon. **11**, 441 (2017).
[20] H. J. Caulfield and S. Dolev, Nat. Photon. **4**, 261 (2010).
[21] E. Kuramochi, K. Nozaki, A. Shinya, K. Takeda, T. Sato, S. Matsuo, H. Taniyama, H. Sumikura, and M. Notomi, Nat. Photon. **8**, 474 (2014).
[22] J. Lee, S. Pak, Y. W. Lee, Y. Cho, J. Hong, P. Giraud, H. S. Shin, S. M. Morris, J. I. Sohn, S. N. Cha, and J. M. Kim, Nat. Commun. **8**, 14734 (2017).
[23] M. D. Tran, H. Kim, J. S. Kim, M. H. Doan, T. K. Chau, Q. A. Vu, J. H. Kim, and Y. H. Lee, Adv. Mater. **31**, 1807075 (2019).
[24] S. Gao, G. Liu, H. Yang, C. Hu, Q. Chen, G. Gong, W. Xue, X. Yi, J. Shang, and R. W. Li, ACS Nano **13**, 2634 (2019).
[25] Z. G. Cheng, C. Rios, W. H. P. Pernice, C. D. Wright, and H. Bhaskaran, Sci. Adv. **3**, e1700160 (2017).
[26] J. Feldmann, N. Youngblood, C. D. Wright, H. Bhaskaran, and W. H. P. Pernice, Nature (London) **569**, 208 (2019).
[27] H. S. P. Wong, S. Raoux, S. B. Kim, J. Liang, J. P. Reifenberg, B. Rajendran, M. Asheghi, and K. E. Goodson, Proc. IEEE **98**, 2201 (2010).
[28] K. Buse, Appl. Phys. B **64**, 391 (1997).
[29] H. G. Li, Z. Q. Cao, H. F. Lu, and Q. S. Shen, Appl. Phys. Lett. **83**, 2757 (2003).
[30] H. Dai, C. Yin, X. Ye, B. Jiang, M. Ran, Z. Cao, and X. Chen, Sci. Rep.-UK **7**, 3174 (2017).
[31] Y. L. Zheng, W. Yuan, X. F. Chen, and Z. Q. Cao, Opt. Express **20**, 9409 (2012).
[32] H. F. Lu, Z. Q. Cao, H. G. Li, and Q. S. Shen, Appl. Phys. Lett. **85**, 4579 (2004).
[33] H. L. Dai, Y. H. Jiao, Z. C. Sun, Z. Q. Cao, and X. F. Chen, Biomed. Opt. Express **9**, 4149 (2018).
[34] G. Chen, Z. Q. Cao, J. H. Gu, and Q. S. Shen, Appl. Phys. Lett. **89**, 081120 (2006).
[35] C. Ríos, M. Stegmaier, P. Hosseini, D. Wang, T. Scherer, C. D. Wright, H. Bhaskaran, and W. H. P. Pernice, Nat. Photon. **9**, 725 (2015).
[36] H. K. He, R. Yang, W. Zhou, H. M. Huang, J. Xiong, L. Gan, T. Y. Zhai, and X. Guo, Small **14**, 1800079 (2018).